Tunable zero-field superconducting diode effect in two-dimensional ferromagnetic/superconducting $Fe_3GeTe_2/NbSe_2$ heterostructure

Guojing Hu[1,§], Yechao Han[2,§], Weiqi Yu[1], Senhao Lv[1], Yuhui Li[1,2], Zizhao Gong[1], Hui Guo[1,2], Ke Zhu[1,2], Zhen Zhao[1,2], Qi Qi[1,2], Guoyu Xian[1,2], Lihong Bao[1,2,3 ✉], Xiao Lin[2], Jinbo Pan[1,2 ✉], Shixuan Du[1,2], Haitao Yang[1,2,3 ✉], and Hong-Jun Gao[1,2,3]

[1] Beijing National Center for Condensed Matter Physics and Institute of Physics, Chinese Academy of Sciences, Beijing 100190, China
[2] School of Physical Sciences, University of Chinese Academy of Sciences, Beijing 100049, China
[3] Songshan Lake Materials Laboratory, Dongguan 523808, China
[§] Guojing Hu and Yechao Han contributed equally to this work.

ABSTRACT: The emergence of superconducting diode effect (SDE) provides a new platform to investigate the intertwining among band topology, superconductivity, and magnetism, thereby establishing the foundation for achieving ultra-low dissipation devices and circuits. The realization of the tunable zero-field SDE in two-dimension (2D) devices is significant for 2D circuits, however, there has been great challenges in the appropriate materials synergy and fine device design. Here, we report a zero-field SDE in the van der Waals (vdW) heterostructure constructed by the Ising superconducting $NbSe_2$ and ferromagnetic Fe_3GeTe_2 with a large perpendicular magnetic anisotropy. Based on the valley-Zeeman spin-orbit interaction (SOI) in $NbSe_2$, the magnitude and polarity of the zero-field SDE can be modulated by altering the ferromagnetic properties of Fe_3GeTe_2 through the application of pre-magnetized out-of-plane magnetic fields. Furthermore, the stable half-wave rectification of square-wave currents is achieved by utilizing the tunable zero-field SDE in the Josephson junction-free structure. The tunable zero-field SDE in 2D heterostructures brings new opportunities for understanding the coexistence of superconductivity and time-reversal symmetry breaking, and for fabricating 2D ultra-low dissipation circuits.

KEYWORDS: zero-field superconducting diode effect, Ising superconducting $NbSe_2$, ferromagnetic Fe_3GeTe_2, half-wave rectification
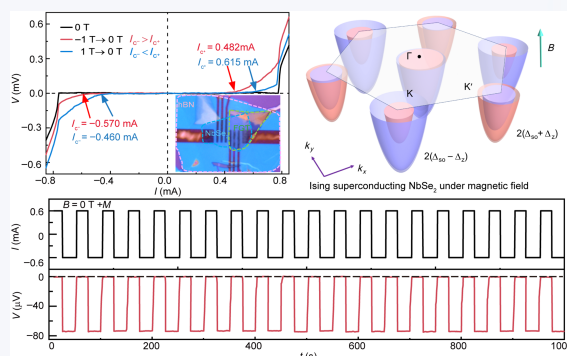
1 Introduction

Superconducting diode effect (SDE) is a novel phenomenon in the superconducting transport, analogous to the non-reciprocal charge transport in semiconductor diodes. It refers to a system allowing supercurrent to flow only in one direction, while exhibiting a finite resistance in the opposite direction [1–3]. This characteristic renders SDE promising for a wide range of applications in ultra-low dissipation circuits, offering new opportunities for superconducting electronics, superconducting spintronics, and quantum information technologies. Simultaneous breaking of inversion and time-reversal symmetries constitutes an essential prerequisite for realizing SDE [4–6]. Consequently, the search for new systems generating SDE and exploring its underlying physical mechanisms has attracted considerable attention. To date, SDE has been observed in a diverse array of superconducting systems [7–9]. However, most of observed SDE require external magnetic fields to break the time-reversal symmetry, encompassing non-centrosymmetric superconductors like MoS_2 [10], $NbSe_2$ [11, 12], Josephson junctions $Al/InAs$–2DEG/Al [13], $Nb/NiTe_2/Nb$ [14], as well as specialized configurations such as the twisted graphene [15, 16], WS_2 nanotubes [17], and $Bi_2Te_3/FeTe$ systems [18]. The field-induced SDE in these systems could restrict the practical applications in the future [19].

The exploration of the zero-field SDE has garnered significant attention, with experimental reports of such systems emerging

successively [20–22], including the non-centrosymmetric superconducting/ferromagnetic multilayers [2, 23, 24], the lateral Nb/[Pt/$Y_3Fe_5O_{12}$]/Nb Josephson junction with a Rashba-type barrier [25], and the vertical $NbSe_2$/Nb_3Br_8/$NbSe_2$ Josephson junction with a polarized barrier [26]. Most of the observed zero-field SDEs in these systems involve complicated device geometries and different generation mechanisms. Hence, the exploration of simple device configurations and new generation mechanisms to achieve the zero-field SDE sparks wide interests recently. Leveraging the proximity effect in superconducting/ferromagnetic heterostructures offers a new avenue for achieving a field-free SDE [27–29]. At the interface of high-quality superconducting/ ferromagnetic systems, the magnetic exchange interaction of the ferromagnetic layer permeates into the superconducting layer, thereby breaking the time-reversal symmetry of the superconducting material, akin to the influence of an externally applied magnetic field [30, 31]. In fact, the magnetic proximity induced spin-splitting of quasi-particle states has been documented in EuS/Al [32] and EuO/Al thin-film systems [33, 34], and a superconducting vortex diode effect has been observed in the Nb/EuS thin-film system [35]. In comparison to superconducting/ ferromagnetic thin film systems, ferromagnetic/superconducting vdW heterostructures lack dangling bond connections between layers, thereby circumventing common issues such as defects, lattice mismatch, and atomic interdiffusion encountered in thin film samples [36, 37]. However, owing to the weak vdW forces, interactions between distinct vdW materials are comparatively diminished, posing a challenge for the realization of zero-field SDE in ferromagnetic/superconducting vdW heterostructures via the magnetic proximity effect or localized stray fields, and this avenue remains unexplored.

Here, we have engineered a ferromagnetic/superconducting Fe_3GeTe_2 (FGT)/$NbSe_2$ bilayer vdW heterostructure by utilizing the Ising superconductivity of $NbSe_2$ and the large perpendicular magnetic anisotropy of ferromagnetic FGT. As a result of the broken time-reversal symmetry induced by the magnetic effect of the ferromagnetic FGT, a zero-field SDE has been observed in the FGT/$NbSe_2$ bilayer vdW heterostructure, where combined effect of the broken inversion symmetry and spin-orbit interaction (SOI) endow the few-layer $NbSe_2$ with Ising superconductivity. The emergence of the zero-field SDE in the FGT/$NbSe_2$ bilayer vdW heterostructure stems from the valley-Zeeman SOI of the Ising superconducting $NbSe_2$, and its magnitude and polarity can be modulated by utilizing the distinct magnetic states of Fe_3GeTe_2 under different pre-magnetized out-of-plane magnetic fields. Furthermore, a stable superconducting half-wave rectification of a square-wave excitation is demonstrated under various pre-magnetized magnetic fields. The realization of the zero-field SDE in the FGT/$NbSe_2$ bilayer vdW heterostructure offers direct evidence for the coexistence of superconductivity and time-reversal symmetry breaking at the microscopic level, potentially resulting in the emergence of the finite-momentum Cooper pairs. Furthermore, the ferromagnetic/superconducting FGT/$NbSe_2$ vdW heterostructure with the tunable zero-field SDE provides a new platform for the development of two-dimensional (2D) ultra-low dissipation circuits.

2   Results and discussion

As depicted in Fig. 1(a) illustrating the atomic structure, the in-

plane inversion symmetry of monolayer $NbSe_2$ is disrupted because the Nb and Se sites are not equivalent. The combination of broken inversion symmetry and large SOI can generate an effective Zeeman field H_{SO} perpendicular to the plane, which leads to the spin splitting at the K, and its inversion partner K', and locks the spins near K and K' to be parallel to the c axis of the monolayer. This spin-momentum locking results in the in-plane upper critical field far exceeding the Pauli paramagnetic limit, characterized as Ising superconductivity [38–40]. However, such a spin-momentum locking just appears in the monolayer or the few-layer $NbSe_2$, while is absent in the multilayer or bulk form. In the Ising superconducting $NbSe_2$, only the inversion symmetry is broken, while the time-reversal symmetry remains preserved. Figure 1(b) illustrates the band structure of $NbSe_2$, featuring a pocket at the Γ point of the Brillouin zone and two pockets splitting at the K and K' points. Upon the application of an out-of-plane magnetic field, the time reversal symmetry of $NbSe_2$ can be broken, leading to the spin splitting of $2(\Delta_{SO} + \Delta_Z)$ and $2(\Delta_{SO} - \Delta_Z)$ at the K and K' points, respectively, as the consequence of the interplay between the spin-momentum locking and Zeeman effect. Consequently, the BCS-type zero-momentum Cooper pairing (symmetric around Γ point) becomes asymmetric around the Γ point, leading to a Fulde–Ferrell–Larkin–Ovchinnikov (FFLO)-type finite-momentum Cooper pairing in Ising-type superconducting states, thus generating the nonreciprocity of supercurrent. Experimentally, SDE and the magnetic chiral anisotropy have been observed in devices of the few-layer $NbSe_2$ when subjected to out-of-plane magnetic fields [11, 12].

Inspired by the findings, we constructed a ferromagnetic/superconducting bilayer vdW heterostructure composed of the ferromagnetic FGT and Ising superconducting $NbSe_2$, and explored its nonreciprocal transport characteristics. The FGT and $NbSe_2$ crystals are synthesized using a chemical vapor transport (CVT) method. As depicted in Fig. S1 in the Electronic Supplementary Material (ESM), X-ray diffraction (XRD) patterns of both FGT and $NbSe_2$ crystals exhibit the characteristic diffraction peaks of (00l), indicating their orientation along the c-axis direction and high crystalline quality. Scanning electron spectroscopy (SEM) equipped with energy-dispersive X-ray spectroscopy (EDS) confirms the perfect stoichiometric ratio of FGT and $NbSe_2$ crystals (Fig. S2 in the ESM). The magnetic measurement results demonstrate the ferromagnetic properties of FGT with a Curie temperature of 220 K and the significant perpendicular magnetic anisotropy (Fig. S3 in the ESM). As depicted in the Fig. 1(c), to eliminate the influence of the $NbSe_2$ thickness and device geometry on experimental accuracy and facilitate a clear comparison of the magnetic effect of the ferromagnetic FGT on the few-layer $NbSe_2$, we engineered two distinct measurement channels for heterostructure devices using the same few-layer $NbSe_2$ nanosheet: One channel comprises pure $NbSe_2$ (Ch1), while the other features the FGT/$NbSe_2$ bilayer vdW heterostructure (Ch2). Optical images of the heterostructure devices featuring the two distinct channels are presented in Fig. 1(d), where the thicknesses of $NbSe_2$ and FGT are determined to approximately 5 and 9 nm, corresponding to approximately 7 and 11 layers, respectively. As shown in the optical image of Ch2, the FGT layer almost completely covers the underlying $NbSe_2$ layer. Therefore, the out-of-plane direction stray field generated by the magnetization of FGT layer exerts a negligible effect on $NbSe_2$ layer. In addition, the resistivity of FGT and normal-
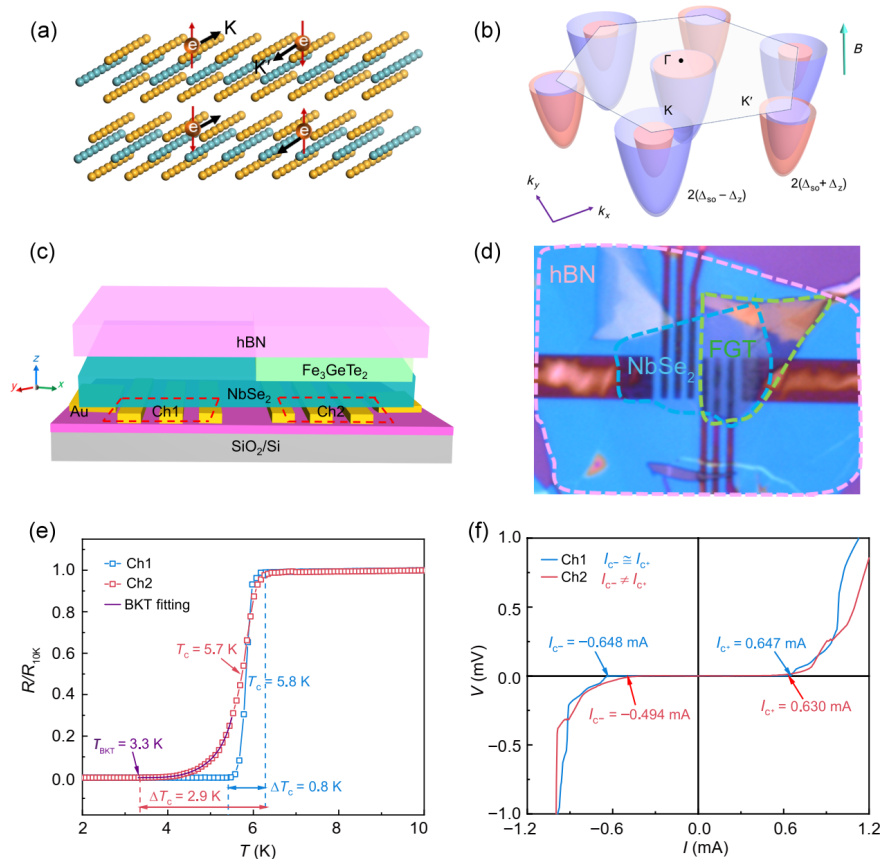
Figure 1 (a) Illustration of the spin–momentum locking in the few-layer NbSe$_2$. (b) Schematic band structure of the few-layer NbSe$_2$. The combination of SOI and the broken inversion symmetry of the few-layer NbSe$_2$ causes the valley-dependent spin splitting and locking. When a magnetic field is applied perpendicular to *ab* plane, the combination of the spin-momentum locking and Zeeman effect can result in the further spin splitting 2($\Delta_{SO} + \Delta_Z$) and 2($\Delta_{SO} - \Delta_Z$) between the K and K′ points. The band structures of the spin branches are plotted with different colors. (c) Schematic illustration of the heterostructure device with a two-channel structure: the channel of the few-layer NbSe$_2$ (Ch1) and the channel of FGT/NbSe$_2$ bilayer heterostructure (Ch2). (d) Optical image of the heterostructure device with the two-channel structure. The blue dashes surround the whole NbSe$_2$ layer, the green dashes surround the FGT layer, and the pink dashes define the top hBN layer. (e) Temperature dependence of Ch1 and Ch2 by a four-terminal measurement. The purple solid line represents the BKT transition using the Halperin–Nelson equation for fitting, which gives a T_{BKT} = 3.3 K. (f) *I–V* curves of Ch1 and Ch2 at 2 K under the zero magnetic field with the pre-magnetization by applying a magnetic field of 1 T.

state NbSe$_2$ are calculated to be 6.7 × 10^{-7} and 4.3 × 10^{-8} Ω·m, indicating that the current predominantly flows through the NbSe$_2$ layer. Consequently, the shunting effect of FGT can be neglected in the transport measurement.

The superconducting critical temperatures (T_c) of the few-layer NbSe$_2$ and FGT/NbSe$_2$ bilayer vdW heterostructure can be determined to be 5.8 and 5.7 K according to the temperature-dependent resistance (*R–T*) curves of Ch1 and Ch2, which exhibit a slight difference. However, a notable difference is observed in the superconducting transition zones from the normal state to the zero-resistance state, defined as ΔT_c: Ch1 shows a sharp superconducting transition of 0.8 K, whereas Ch2 exhibits a broad superconducting transition zone of 2.9 K. This observation suggests that the magnetization of ferromagnetic FGT can affect the pairing of vortices and antivortices in NbSe$_2$, thereby broadening the transition range from the normal state to the zero-resistance state. The tail of *R–T* curve in Ch2 can be fitted using the Halperin–Nelson equation describing the Berezinskii–Kosterlitz–Thouless (BKT) transition [41–43]

$$R = R_0 e^{\left(-2b\left(\frac{T_{c0}-T}{T-T_{BKT}}\right)^{\frac{1}{2}}\right)}$$

The R_0 and *b* in the equation are material-dependent parameters. The fitting result, depicted by the purple solid line in Fig. 1(e), yields T_{BKT} = 3.3 K, indicating the onset of a zero-resistance state driven by vortex–antivortex pairs below 3.3 K. Moreover, the current–voltage characteristics (*I–V*) curves of the Ch1 and Ch2 at the zero magnetic field after the pre-magnetization in a positive out-of-plane magnetic field at 2 K were measured. The critical current is defined as the *d.c.* current bias at the onset of voltage, where I_{c+} and I_{c-} represent the critical currents in the positive and negative current directions, respectively. As shown in Fig. 1(f), I_{c+} and I_{c-} in Ch1 are essentially equal, while I_{c+} in Ch2 is substantially larger than I_{c-}, indicating a highly direction-dependent critical current behavior in Ch2, known as the nonreciprocal behavior.

Figure 2(a) displays the *I–V* curves of Ch2 measured at the zero magnetic field after the pre-magnetization in different out-of-plane magnetic fields at 2 K. The difference between I_{c+} and I_{c-} is small without a pre-magnetization process, while I_{c+} and I_{c-} show an obvious non-reciprocal behavior when applying a pre-magnetized out-of-plane magnetic field. The *I–V* curves swept upwards and downwards do not exhibit a significant change, suggesting the difference between the breaking and the retrapping critical current is not the reason for the non-reciprocal behavior (inset of Fig. 2(a)). Furthermore, after the pre-magnetization with a positive (negative)
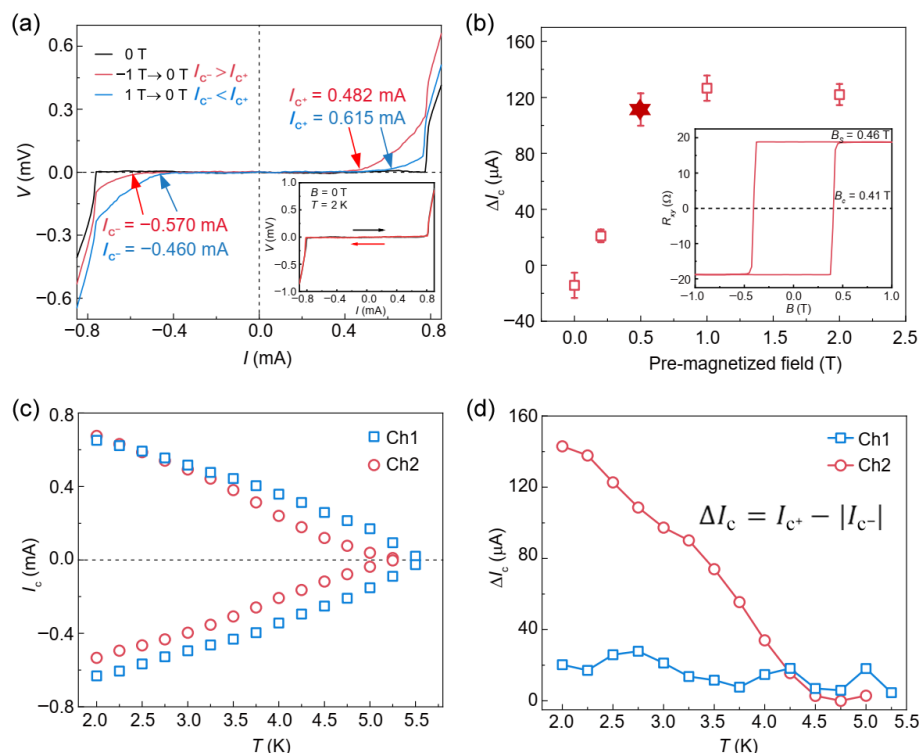
Figure 2 (a) I–V curves of Ch2 with the pre-magnetization by applying different out-of-plane magnetic fields, and the arrows mark the critical currents. The inset shows the I–V curve with a different current sweep direction at the zero magnetic field without the pre-magnetization, where the arrows with the corresponding color indicate the current sweep direction. (b) Pre-magnetized magnetic field dependence of non-reciprocal component ΔI_c, the non-reciprocal component of critical current was calculated by $\Delta I_c = |I_{c^+} - |I_{c^-}||$. The inset exhibits the magnetic field-dependent Hall resistance of a Fe_3GeTe_2 nanosheet with thickness of 9 nm, where the saturation field and coercive field of the FGT nanosheet are 0.46 and 0.41 T. (c) Temperature dependence of critical current I_c in Ch1 and Ch2. (d) Temperature dependence of ΔI_c in Ch1 and Ch2.

out-of-plane magnetic field, I_{c^+} is much larger (smaller) than I_{c^-}, indicating that the non-reciprocity in Ch2 can be reversed by applying pre-magnetized magnetic fields. This observation demonstrates that the underlying time-reversal-symmetry-breaking order can be efficiently modulated by a pre-magnetized out-of-plane magnetic field.

To further explore the relationship between non-reciprocity and pre-magnetized out-of-plane magnetic fields, the non-reciprocal component of the critical current $\Delta I_c = I_{c^+} - |I_{c^-}|$ at the zero magnetic field is plotted against the pre-magnetized out-of-plane filed in Fig. 2(b). ΔI_c monotonically increases with the increasing of the pre-magnetized magnetic field, and remains basically invariable at 0.5 T, where the pre-magnetized magnetic field is corresponding to the saturation field of FGT with the thickness of 9 nm (inset of Fig. 2(b), Fig. S4 in the ESM). The result reveals that the zero-field non-reciprocity of $NbSe_2$ originates from the magnetic effect of the ferromagnetic FGT, wherein the magnitude or direction of the magnetic moments in FGT layer can be controlled by applying a pre-magnetized magnetic field. Temperature-dependent critical current I_c and non-reciprocal component ΔI_c in Ch1 and Ch2 are also investigated. I_c in both Ch1 and Ch2 monotonically decreases as the temperature increases, while ΔI_c in Ch1 and Ch2 exhibits different behaviors with the temperature increasing. ΔI_c of Ch2 is much larger than that of Ch1, and monotonically decreases as the temperature increases, whereas ΔI_c of Ch1 remain unchanged and is negligible, indicating the absence of a zero-field non-reciprocal behavior in Ch1.

Figure 3 shows the magnetic field dependencies of SDE in Ch2.

Here, the magnetic field was initially set to 1 T, far exceeding the coercive field of FGT. Subsequently, the I–V curves of Ch2 are recorded while sweeping the magnetic field from –0.2 to +0.2 T at 2 K. I_c (Fig. 3(a)) and ΔI_c (Fig. 3(b)) are plotted against the magnetic fields. ΔI_c reaches a positive maximum peak at approximately 0.001 T, and approaches zero at +0.008 T. With a further increase in the magnetic field, the sign of ΔI_c reverses, and reaches a negative dip at approximately +0.01 T. After saturating the magnetization of FGT by applying an initial magnetic field of –1 T, the I–V curves of Ch2 are also measured by sweeping the magnetic field from –0.2 to +0.2 T at 2 K to obtain the magnetic field dependencies of I_c and ΔI_c. As shown in Figs. 3(c) and 3(d), ΔI_c reaches a positive maximum peak at approximately –0.01 T, and approaches zero at –0.006 T. The sign of ΔI_c reverses and reaches a negative maximum dip at approximately –0.001 T. The magnetic field under which ΔI_c reaches its maximum in both processes is close to the zero field, and the sign of ΔI_c is correlated to the direction of the pre-magnetized magnetic fields. This observation implies that the underlying time-reversal symmetry breaking in the FGT/$NbSe_2$ bilayer vdW heterostructure stems from the magnetic effect of the ferromagnetic FGT layer. Moreover, we investigated the characteristics of the Ising superconducting $NbSe_2$ when coupled with an FGT layer through first-principles calculations. The spin-resolved projected band structures from Γ to K point and K′ point of the FGT/$NbSe_2$ heterostructure are depicted in Figs. 3(e) and 3(f). The red and blue bands corresponding to the top layer $NbSe_2$ illustrate the band splitting occurring at the Γ, time-reversal related K and K′ points, when the magnetizations of FGT point upwards (+M). Conversely, when the FGT magnetization point downwards (–M), the points Γ,
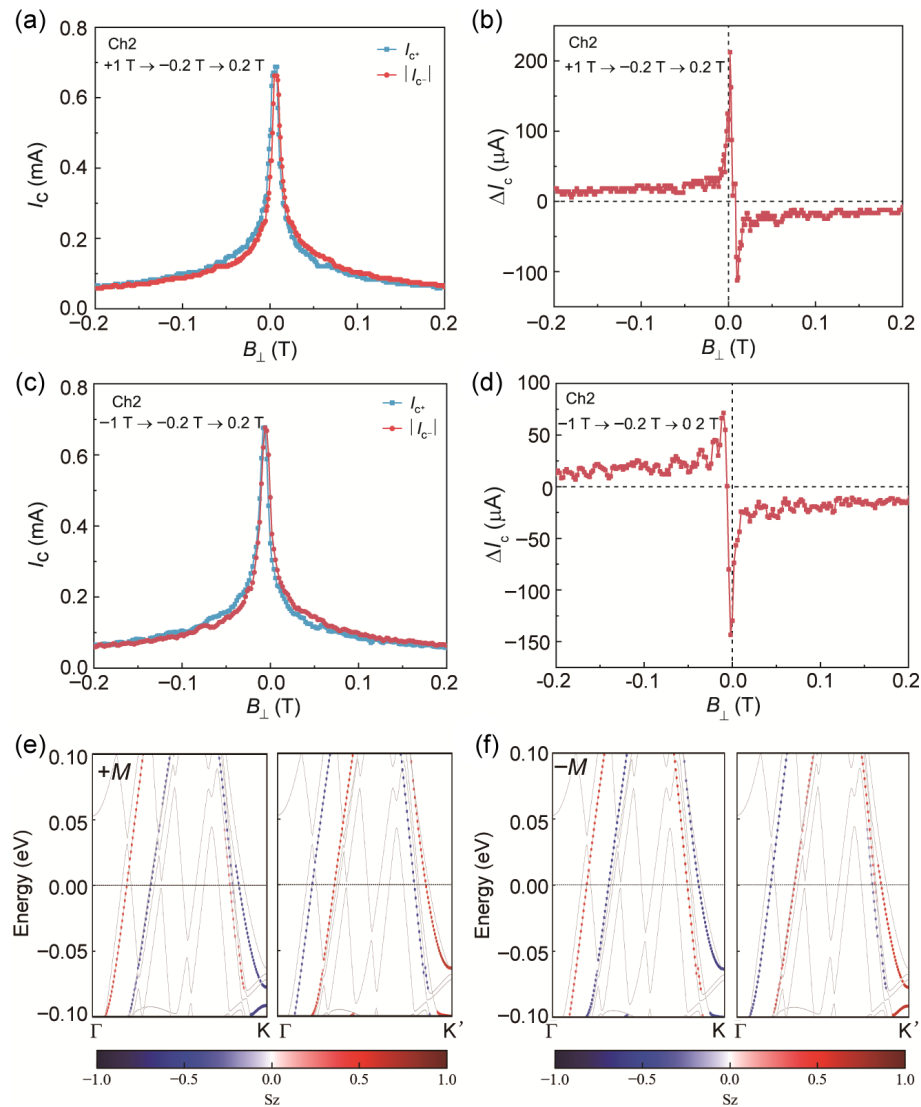
Figure 3 Magnetic field dependences of SDE. (a) I_c of Ch2 as a function of the magnetic field at 2 K. First, the magnetic field was set to 1 T to perform the pre-magnetization process, then the magnetic field was swept from −0.2 to +0.2 T (upward sweep) for positive (blue) and negative (red) currents. (b) ΔI_c as a function of the magnetic field, corresponding to (a). (c) I_c of Ch2 as a function of the magnetic field at 2 K. First, the magnetic field was set to −1 T to perform the pre-magnetization process, then the magnetic field was swept from −0.2 to +0.2 T (upward sweep) for positive (blue) and negative (red) currents. (d) ΔI_c as a function of the magnetic field, corresponding to (c). (e) Spin-resolved projected band structures of the top NbSe$_2$ monolayer under upward magnetization (+M) of the FGT monolayer along the different high symmetry paths. Here, the whole bands of heterostructure are plotted by the grey line. The bands mainly contributed by the top NbSe$_2$ monolayer are marked with dots colored by the magnitude of spin z-component contribution. (f) Spin-resolved projected band structures of top NbSe$_2$ monolayer under downward magnetization (−M) of the FGT monolayer along the different high symmetry paths.

K, and K′ exhibit a distinct band splitting pattern. The theoretical results strongly support that the observation of the zero-field SDE in the FGT/NbSe$_2$ bilayer heterostructure is attributed to the valley-Zeeman SOI induced by the magnetic effect of the ferromagnetic FGT layer. However, the underlying origin of the observed peak, sign reversal, and the dip in the magnetic field dependence of ΔI_c remains unclear, potentially linked to the evolution of complex magnetic domains and vortices. Additionally, the magnetic field dependencies of I_c and ΔI_c in Ch2 at different temperatures are similar with those in Figs. 3(c) and 3(d) while the maximum value of ΔI_c monotonically decreases with the temperature increasing (Fig. S5 in the ESM). For comparison, I_c (Fig. S6(a) in the ESM) and ΔI_c (Fig. S6(b) in the ESM) in Ch1 are plotted against the sweeping magnetic fields at 2 K. ΔI_c in Ch1 approaches zero at 0 T and reaches a maximum at 0.04 T, demonstrating a field-induced non-

reciprocal behavior.

To further elucidate the tunable zero-field SDE in Ch2, we conducted experiments to investigate its half-wave rectification response under various pre-magnetized magnetic fields (Fig. 4). Applying an out-of-plane magnetic field of 1 T for pre-magnetization resulted in the positive magnetization of FGT, where I_{c+} is larger than I_{c-}. Subsequently, when a square-wave excitation current of 0.65 mA, exceeding I_{c-} but below I_{c+}, is applied to the device. As shown in Fig. 4(a), the positive half-cycle of the current exhibits a superconducting state, while the negative half-cycle displayed a voltage drop, leading to the rectification. Conversely, the pre-magnetization with a magnetic field of −1 T gives rise to the negative magnetization of FGT, where I_{c-} exceeds I_{c+}. Then the application of a square-wave excitation current of 0.59 mA, surpassing I_{c+} but below I_{c-}, resulted in a voltage drop only during
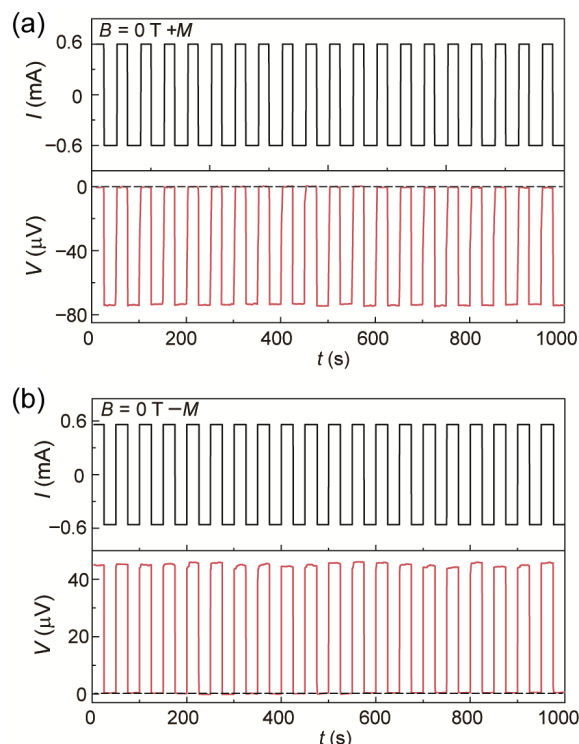
Figure 4 (a) Zero-field SDE of the device after applying the out-of-plane magnetic field of 1 T to perform the pre-magnetization process. At this process, I_{c+} becomes larger than I_{c-}, and a square-wave excitation current 0.6 mA at a frequency of 0.02 Hz was sent through the device. The magnitude of the square-wave excitation current is larger than I_{c-} and smaller than I_{c+}, hence, there is a voltage drop only in the negative half-cycle of the current. (b) Zero-field SDE of the device after applying the pre-magnetization field of –1 T. At this situation, I_{c+} becomes smaller than I_{c+}, and a square-wave excitation current 0.56 mA at a frequency of 0.02 Hz was sent through the device. The magnitude of the square-wave excitation current is larger than I_{c+} and smaller than I_{c-}, hence, there is a voltage drop only in the positive half-cycle of the current.

the positive half-cycle of the current (Fig. 4(b)). The observed half-wave rectification at the zero field demonstrates diode behavior in Ch2.

Before closing, we discuss the possible origin of the zero-field SDE observed in Ch2. In presence of the time-reversal breaking, the combined effect of broken inversion symmetry and Rashba or Ising spin-orbit coupling (SOC) can induce the finite-momentum Cooper pairing to generate the nonreciprocal supercurrent. In the FGT/NbSe$_2$ bilayer vdW heterostructure, the nonreciprocity of supercurrent can stem from either Ising SOC of NbSe$_2$ or Rashba SOC at the vdW interface. However, for Ising SOC of NbSe$_2$, the Cooper pairing between two electrons has the opposite momentum and opposite out-of-plane spin polarization spins, which require an out-of-plane magnetic field or magnetization that is parallel to the spin orientation of the electron to induce a FFLO-type finite-momentum Cooper pairing, thus generating the nonreciprocity of supercurrent. As for Rashba SOC at the interface, the Cooper pairing between two electrons has the opposite momentum and opposite in-plane spin polarization, where an in-plane magnetic field or magnetization can lead to a FFLO-type finite-momentum Cooper pairing to give rise to SDE [44]. As shown in Fig. S7 in the ESM, we conducted the measurements of the I–V curves of Ch2 at the zero filed when applying an in-plane magnetic field to the pre-magnetization, which did not yield any significant nonreciprocal

behavior. On the contrary, the nonreciprocity of supercurrent can be effectively governed by the pre-magnetization with an out-of-plane magnetic field. These findings strongly suggest that the zero-field SDE in the FGT/NbSe$_2$ bilayer vdW heterostructure is not caused by Rashba SOC at the interface, but by Ising SOC of the few-layer NbSe$_2$. Furthermore, the magnitude of ΔI_c monotonically increases with increasing the pre-magnetized magnetic field, and remains basically invariable at 0.5 T, where the pre-magnetized magnetic field is corresponding to the saturation field of FGT with the thickness of 9 nm. Additionally, its sign can be reversed by altering the direction of the pre-magnetized magnetic field. The tunable zero-field SDE implies that the underlying time-reversal symmetry breaking in the FGT/NbSe$_2$ bilayer vdW heterostructure stems from the magnetic effect of the ferromagnetic FGT layer. The first-principles calculations also confirm the different band splitting occurring at the Γ, K, and K′ points for NbSe$_2$ when the magnetizations of FGT point upwards or downwards. This conjecture is consistent with the recent theoretical calculation results conducted by Zhang's research group [45], which further support the magnetic effect of the ferromagnetic FGT layer induced the time-reversal symmetry breaking in the FGT/NbSe$_2$ bilayer vdW heterostructure.

3 Conclusions

In conclusion, our experimental results have demonstrated the emergence of a zero-field SDE in ferromagnetic/superconducting FGT/NbSe$_2$ bilayer vdW heterostructure, achieved through the effect of a ferromagnetic FGT layer induced time-reversal symmetry breaking in the Ising superconducting NbSe$_2$ layer. The appearance of the zero-field SDE is attributed to the valley-Zeeman SOI in the few-layer NbSe$_2$, and its magnitude and polarity can be regulated by applying pre-magnetized out-of-plane magnetic fields. Furthermore, the stable half-wave rectification of square-wave currents is performed by employing the tunable zero-field SDE in the Josephson junction-free structure. The observation of the zero-field SDE in the FGT/NbSe$_2$ vdW heterostructure provides the direct evidence of the microscopic coexistence between the superconductivity and broken time-reversal symmetry, potentially giving rise to the finite-momentum Cooper pairing. Additionally, the realization of the tunable zero-field SDE in the Josephson junction-free 2D system presents novel prospects for the advancement of all-2D ultra-low dissipation circuits.

4 Experimental section

4.1 Single crystal growth

The FGT and NbSe$_2$ single crystals were both grown by a CVT method. The specific steps of the CVT growth process were as follows. A stoichiometric amount of high-purity element (molar ratio Fe:Ge:Te = 3:1:2, molar ratio Nb:Se = 1:2) were mixed and poured into an quartz tube together with iodine (4 mg/cm^3) as a transport agent. The quartz tubes were evacuated to 10^{-4} Pa and sealed with oxyacetylene. Then the sealed quartz tubes were placed into the two-zone tubular furnace, and the temperatures of the source and growth zones were raised to target temperature with an appropriate rate. For the Fe$_3$GeTe$_2$ (NbSe$_2$) single crystals, the temperatures of the source and growth zones were raised to 750 °C (850 °C) and 650 °C (750 °C) with 2 °C/min, and maintained at

750/650 °C (850/750 °C) for two weeks. The furnace was cooled to room temperature naturally, and the resulting shiny crystals were collected.

4.2 Characterization techniques

The crystal structures of FGT and $NbSe_2$ were characterized by XRD. The stoichiometric ratio was determined by the SEM equipped with EDS. The magnetization of the crystal was measured by a SQUID magnetometer (Quantum Design MPMS-3). The thickness of Fe_3GaTe_2 was determined by using a commercial Cypher S AFM (Oxford Instruments, Asylum Research, Santa Barbara, USA).

4.3 Electrode processing

The bottom electrode configuration consisting of two parallel four electrodes was patterned on a SiO_2/Si substrate by electron beam lithography with the deposition of Cr/Au (3/12 nm) metal through thermal evaporation. After lift-off process, the metal electrodes were obtained.

4.4 Device fabrication

Mechanical exfoliation and dry transfer processes were performed in a glove box (O_2, H_2O < 0.1 ppm). To better solve the problem of residual glue in the dry transfer process, we treated the polydimethylsiloxane (PDMS) by soaking it in isopropanol solution for one week, and then drying it naturally. Using the processed PDMS to transfer sample can significantly reduce the residual adhesive on the surface of the sample. Firstly, we transferred the desired $NbSe_2$ nanoflake onto the parallel electrodes, where the $NbSe_2$ nanoflake covered the electrodes of two test channels. Then a layer of FGT was only stacked onto the right side of the four parallel electrodes, covering one test channel. Finally, a layer of hBN was utilized to encapsulate heterostructure for protection.

4.5 Electrical transport measurements

The electric transport measurements were carried out in a Quantum Design Physical Property Measurement System (PPMS) using a Keithley 6221 current source and a Keithley 2182 A nanovoltmeter. The resistance–temperature (R–T) curves, current–voltage characteristic (I–V) curve, differential conductance resistance (dV/dI), and the half-wave rectification were measured with a four-probe configuration.

4.6 First-principles calculations

First-principles calculations were performed with Vienna *ab initio* Simulation Package (VASP), based on Kohn–Sham density functional theory (DFT) [46, 47]. The projector augmented-wave (PAW) pseudopotentials were adopted to describe the electron-ion interaction with a plane-wave cutoff of 500 eV [48]. The Perdew-Burke-Ernzerhof generalized gradient approximation (PBE-GGA) was employed to deal with the electron exchange-correlation energy [49]. The FGT/$NbSe_2$ heterostructure was constructed by stacking an FGT monolayer on a 2H-$NbSe_2$ bilayer. Considering the lattice mismatch, a $\sqrt{3} \times \sqrt{3}$-FGT supercell and a 2×2-$NbSe_2$ supercell in x-y plane were adopted with a lattice mismatch less than 1%. DFT-D3 method of Grimme [50] was used to correct the vdW interactions. The most stable staking structure of FGT/$NbSe_2$ heterostructure was considered in accordance with Ref. [45]. Considering SOC effect, the band structures mainly contributed by the top $NbSe_2$ monolayer closest to Fe_3GeTe_2 were marked with

dots colored by the magnitude of spin z-component contribution. A band wavefunction ψ_{nk} was thought to be mainly contributed by the top $NbSe_2$ monolayer, if the projection weight of the top $NbSe_2$ monolayer was higher than the other two layers.

4.7 Data processing

The critical current was defined as the *d.c.* current bias at the onset of voltage in the I–V curves, where the I_{c+} and I_{c-} represent the critical currents in the positive and negative current directions, respectively. The order of magnitude of the error of the critical currents was about ±0.026 mA (3%). The superconducting transition temperature (T_c) was defined as the temperature where the resistance reached half of the normal resistance.

Data availability

All data needed to support the conclusions in the paper are presented in the manuscript and the Electronic Supplementary Material. Additional data related to this paper may be requested from the corresponding author upon request.

Acknowledgements

Declaration of competing interest

All the contributing authors report no conflict of interests in this work.

Author contribution statement

G. J. H.: Data curation, project administration, validation, writing manuscript, experimental design. Y. C. H.: Data curation, project administration, validation, experimental design. W. Q. Y.: Project administration, validation. S. H. L.: Data curation, validation. Y. H. L.: Data curation, validation. Z. Z. G.: Data curation, validation. H. G.: Project administration, writing manuscript. K. Z.: Project administration, writing manuscript. Z. Z.: Project administration, writing manuscript. Q. Q.: Project administration, writing manuscript. G. Y. X.: Project administration, writing manuscript. L. H. B.: Project administration, funding acquisition. X. L.: Project administration, funding acquisition. J. B. P.: Project administration, funding acquisition. S. X. D.: Project administration, funding acquisition. H. T. Y.: Project administration, funding acquisition, writing manuscript. H.-J. G.: Project administration, funding acquisition.

Use of AI statement

None.

References

[1] Hu, J. P.; Wu, C. J.; Dai, X. Proposed design of a josephson diode. *Phys. Rev. Lett.* **2007**, *99*, 067004.

[2] Ando, F.; Miyasaka, Y.; Li, T.; Ishizuka, J.; Arakawa, T.; Shiota, Y.; Moriyama, T.; Yanase, Y.; Ono, T. Observation of superconducting diode effect. *Nature* **2020**, *584*, 373–376.

[3] Nadeem, M.; Fuhrer, M. S.; Wang, X. L. The superconducting diode effect. *Nat. Rev. Phys.* **2023**, *5*, 558–577.

[4] Daido, A.; Ikeda, Y.; Yanase, Y. Intrinsic superconducting diode effect. *Phys. Rev. Lett.* **2022**, *128*, 037001.

[5] Davydova, M.; Prembabu, S.; Fu, L. Universal Josephson diode effect. *Sci. Adv.* **2022**, *8*, eabo0309.

[6] Zhang, Y.; Gu, Y. H.; Li, P. F.; Hu, J. P.; Jiang, K. General theory of josephson diodes. *Phys. Rev. X* **2022**, *12*, 041013.

[7] Hou, Y. S.; Nichele, F.; Chi, H.; Lodesani, A.; Wu, Y. Y.; Ritter, M. F.; Haxell, D. Z.; Davydova, M.; Ilić, S.; Glezakou-Elbert, O. et al. Ubiquitous superconducting diode effect in superconductor thin films. *Phys. Rev. Lett.* **2023**, *131*, 027001.

[8] Ghosh, S.; Patil, V.; Basu, A.; Kuldeep; Dutta, A.; Jangade, D. A.; Kulkarni, R.; Thamizhavel, A.; Steiner, J. F.; von Oppen, F. et al. High-temperature Josephson diode. *Nat. Mater.* **2024**, *23*, 612–618.

[9] Chen, P. B.; Wang, G. Q.; Ye, B. C.; Wang, J. H.; Zhou, L.; Tang, Z. Z.; Wang, L.; Wang, J. N.; Zhang, W. Q.; Mei, J. W. et al. Edelstein effect induced superconducting diode effect in inversion symmetry breaking MoTe$_2$ josephson junctions. *Adv. Funct. Mater.* **2024**, *34*, 2311229.

[10] Wakatsuki, R.; Saito, Y.; Hoshino, S.; Itahashi, Y. M.; Ideue, T.; Ezawa, M.; Iwasa, Y.; Nagaosa, N. Nonreciprocal charge transport in noncentrosymmetric superconductors. *Sci. Adv.* **2017**, *3*, e1602390.

[11] Zhang, E. Z.; Xu, X.; Zou, Y. C.; Ai, L. F.; Dong, X.; Huang, C.; Leng, P. L.; Liu, S. S.; Zhang, Y. D.; Jia, Z. H. et al. Nonreciprocal superconducting NbSe$_2$ antenna. *Nat. Commun.* **2020**, *11*, 5634.

[12] Bauriedl, L.; Bäuml, C.; Fuchs, L.; Baumgartner, C.; Paulik, N.; Bauer, J. M.; Lin, K. Q.; Lupton, J. M.; Taniguchi, T.; Watanabe, K. et al. Supercurrent diode effect and magnetochiral anisotropy in few-layer NbSe$_2$. *Nat. Commun.* **2022**, *13*, 4266.

[13] Baumgartner, C.; Fuchs, L.; Costa, A.; Reinhardt, S.; Gronin, S.; Gardner, G. C.; Lindemann, T.; Manfra, M. J.; Faria Junior, P. E.; Kochan, D. et al. Supercurrent rectification and magnetochiral effects in symmetric Josephson junctions. *Nat. Nanotechnol.* **2022**, *17*, 39–44.

[14] Pal, B.; Chakraborty, A.; Sivakumar, P. K.; Davydova, M.; Gopi, A. K.; Pandeya, A. K.; Krieger, J. A.; Zhang, Y.; Date, M.; Ju, S. L. et al. Josephson diode effect from Cooper pair momentum in a topological semimetal. *Nat. Phys.* **2022**, *18*, 1228–1233.

[15] de Vries, F. K.; Portolés, E.; Zheng, G.; Taniguchi, T.; Watanabe, K.; Ihn, T.; Ensslin, K.; Rickhaus, P. Gate-defined Josephson junctions in magic-angle twisted bilayer graphene. *Nat. Nanotechnol.* **2021**, *16*, 760–763.

[16] Díez-Mérida, J.; Díez-Carlón, A.; Yang, S. Y.; Xie, Y. M.; Gao, X. J.; Senior, J.; Watanabe, K.; Taniguchi, T.; Lu, X.; Higginbotham, A. P. et al. Symmetry-broken Josephson junctions and superconducting diodes in magic-angle twisted bilayer graphene. *Nat. Commun.* **2023**, *14*, 2396.

[17] Qin, F.; Shi, W.; Ideue, T.; Yoshida, M.; Zak, A.; Tenne, R.; Kikitsu, T.; Inoue, D.; Hashizume, D.; Iwasa, Y. Superconductivity in a chiral nanotube. *Nat. Commun.* **2017**, *8*, 14465.

[18] Yasuda, K.; Yasuda, H.; Liang, T.; Yoshimi, R.; Tsukazaki, A.; Takahashi, K. S.; Nagaosa, N.; Kawasaki, M.; Tokura, Y. Nonreciprocal charge transport at topological insulator/superconductor interface. *Nat. Commun.* **2019**, *10*, 2734.

[19] Kim, J. K.; Jeon, K. R.; Sivakumar, P. K.; Jeon, J.; Koerner, C.; Woltersdorf, G.; Parkin, S. S. P. Intrinsic supercurrent non-reciprocity coupled to the crystal structure of a van der Waals Josephson barrier. *Nat. Commun.* **2024**, *15*, 1120.

[20] Kokkeler, T. H.; Golubov, A. A.; Bergeret, F. S. Field-free anomalous junction and superconducting diode effect in spin-split superconductor/topological insulator junctions. *Phys. Rev. B* **2022**, *106*, 214504.

[21] Scammell, H. D.; Li, J. I. A.; Scheurer, M. S. Theory of zero-field superconducting diode effect in twisted trilayer graphene. *2D Mater.* **2022**, *9*, 025027.

[22] Lin, J. X.; Siriviboon, P.; Scammell, H. D.; Liu, S.; Rhodes, D.; Watanabe, K.; Taniguchi, T.; Hone, J.; Scheurer, M. S.; Li, J. I. A. Zero-field superconducting diode effect in small-twist-angle trilayer graphene. *Nat. Phys.* **2022**, *18*, 1221–1227.

[23] Narita, H.; Ishizuka, J.; Kawarazaki, R.; Kan, D.; Shiota, Y.; Moriyama, T.; Shimakawa, Y.; Ognev, A. V.; Samardak, A. S.; Yanase, Y. et al. Field-free superconducting diode effect in noncentrosymmetric superconductor/ferromagnet multilayers. *Nat. Nanotechnol.* **2022**, *17*, 823–828.

[24] Narita, H.; Ono, T. Superconducting diode effect in artificial superlattice. *JSAP Rev.* **2024**, *2024*, 240206.

[25] Jeon, K. R.; Kim, J. K.; Yoon, J.; Jeon, J. C.; Han, H.; Cottet, A.; Kontos, T.; Parkin, S. S. P. Zero-field polarity-reversible Josephson supercurrent diodes enabled by a proximity-magnetized Pt barrier. *Nat. Mater.* **2022**, *21*, 1008–1013.

[26] Wu, H.; Wang, Y. J.; Xu, Y. F.; Sivakumar, P. K.; Pasco, C.; Filippozzi, U.; Parkin, S. S. P.; Zeng, Y. J.; McQueen, T.; Ali, M. N. The field-free Josephson diode in a van der Waals heterostructure. *Nature* **2022**, *604*, 653–656.

[27] Buzdin, A. I. Proximity effects in superconductor-ferromagnet heterostructures. *Rev. Mod. Phys.* **2005**, *77*, 935–976.

[28] Linder, J.; Yokoyama, T.; Sudbø, A. Theory of superconducting and magnetic proximity effect in S/F structures with inhomogeneous magnetization textures and spin-active interfaces. *Phys. Rev. B* **2009**, *79*, 054523.

[29] Linder, J.; Robinson, J. W. A. Superconducting spintronics. *Nat. Phys.* **2015**, *11*, 307–315.

[30] Fulde, P.; Ferrell, R. A. Superconductivity in a strong spin-exchange field. *Phys. Rev.* **1964**, *135*, A550–A563.

[31] De Gennes, P. G. Coupling between ferromagnets through a superconducting layer. *Phys. Lett.* **1966**, *23*, 10–11.

[32] Xiong, Y. M.; Stadler, S.; Adams, P. W.; Catelani, G. Spin-resolved tunneling studies of the exchange field in EuS/Al bilayers. *Phys. Rev. Lett.* **2011**, *106*, 247001.

[33] Strambini, E.; Golovach, V. N.; De Simoni, G.; Moodera, J. S.; Bergeret, F. S.; Giazotto, F. Revealing the magnetic proximity effect in EuS/Al bilayers through superconducting tunneling spectroscopy. *Phys. Rev. Mater.* **2017**, *1*, 054402.

[34] Tedrow, P. M.; Tkaczyk, J. E.; Kumar, A. Spin-polarized electron tunneling study of an artificially layered superconductor with internal magnetic field: EuO-Al. *Phys. Rev. Lett.* **1986**, *56*, 1746–1749.

[35] Gutfreund, A.; Matsuki, H.; Plastovets, V.; Noah, A.; Gorzawski, L.; Fridman, N.; Yang, G.; Buzdin, A.; Millo, O.; Robinson, J. W. A. et al. Direct observation of a superconducting vortex diode. *Nat. Commun.* **2023**, *14*, 1630.

[36] Gibertini, M.; Koperski, M.; Morpurgo, A. F.; Novoselov, K. S. Magnetic 2D materials and heterostructures. *Nat. Nanotechnol.* **2019**, *14*, 408–419.

[37] Gong, C.; Zhang, X. Two-dimensional magnetic crystals and

emergent heterostructure devices. *Science* **2019**, *363*, eaav4450.

[38] Xi, X. X.; Wang, Z. F.; Zhao, W. W.; Park, J. H.; Law, K. T.; Berger, H.; Forró, L.; Shan, J.; Mak, K. F. Ising pairing in superconducting NbSe$_2$ atomic layers. *Nat. Phys.* **2016**, *12*, 139–143.

[39] de la Barrera, S. C.; Sinko, M. R.; Gopalan, D. P.; Sivadas, N.; Seyler, K. L.; Watanabe, K.; Taniguchi, T.; Tsen, A. W.; Xu, X. D.; Xiao, D. et al. Tuning Ising superconductivity with layer and spin-orbit coupling in two-dimensional transition-metal dichalcogenides. *Nat. Commun.* **2018**, *9*, 1427.

[40] Wan, P. H.; Zheliuk, O.; Yuan, N. F. Q.; Peng, X. L.; Zhang, L.; Liang, M. P.; Zeitler, U.; Wiedmann, S.; Hussey, N. E.; Palstra, T. T. M. et al. Orbital Fulde–Ferrell–Larkin–Ovchinnikov state in an Ising superconductor. *Nature* **2023**, *619*, 46–51.

[41] Saito, Y.; Kasahara, Y.; Ye, J. T.; Iwasa, Y.; Nojima, T. Metallic ground state in an ion-gated two-dimensional superconductor. *Science* **2015**, *350*, 409–413.

[42] Hu, G. J.; Wang, C. L.; Wang, S. S.; Zhang, Y.; Feng, Y.; Wang, Z.; Niu, Q.; Zhang, Z. Y.; Xiang, B. Long-range skin Josephson supercurrent across a van der Waals ferromagnet. *Nat. Commun.* **2023**, *14*, 1779.

[43] Huang, C.; Zhou, B. T.; Zhang, H. Q.; Yang, B. J.; Liu, R.; Wang, H. W.; Wan, Y. M.; Huang, K.; Liao, Z. M.; Zhang, E. Z. et al. Proximity-induced surface superconductivity in Dirac semimetal Cd$_3$As$_2$. *Nat. Commun.* **2019**, *10*, 2217.

[44] Wakatsuki, R.; Nagaosa, N. Nonreciprocal current in noncentrosymmetric rashba superconductors. *Phys. Rev. Lett.* **2018**, *121*, 026601.

[45] Yang, Y. T.; Qin, W.; Chen, Y. R.; Zhang, S. H.; Cui, P.; Zhang, Z. Y. Endowing the Ising superconductor NbSe$_2$ with nontrivial band topology via proximity coupling with the two-dimensional ferromagnet Fe$_3$GeTe$_2$. *Phys. Rev. B* **2024**, *109*, L041112.

[46] Kresse, G.; Furthmüller, J. Efficiency of *ab-initio* total energy calculations for metals and semiconductors using a plane-wave basis set. *Comput. Mater. Sci.* **1996**, *6*, 15–50.

[47] Kresse, G.; Furthmüller, J. Efficient iterative schemes for *ab initio* total-energy calculations using a plane-wave basis set. *Phys. Rev. B* **1996**, *54*, 11169–11186.

[48] Blöchl, P. E. Projector augmented-wave method. *Phys. Rev. B* **1994**, *50*, 17953–17979.

[49] Perdew, J. P.; Burke, K.; Ernzerhof, M. Generalized gradient approximation made simple. *Phys. Rev. Lett.* **1996**, *77*, 3865–3868.

[50] Grimme, S. Semiempirical GGA-type density functional constructed with a long-range dispersion correction. *J. Comput. Chem.* **2006**, *27*, 1787–1799.